Energy Advances

ROYAL SOCIETY OF CHEMISTRY

PAPER

View Article Online
View Journal

Cite this: DOI: 10.1039/d6ya00026f

Microporous carbon enhanced by structural modifications to suppress polysulfide shuttling and reduce capacity fading in lithium–sulfur batteries

Delvina Japhet Tarimo, [a] Francisco J. García-Soriano, [b] Alen Vizintin, [b] Christian Prehal, [c] Elena Tchernychova [b] and Volker Presser *[ade]

Commercialization of lithium–sulfur batteries (Li–S) remains complex due to limited cycling stability related to the solubility of polysulfide intermediates, specifically higher-order polysulfides (Li_2S_4 to Li_2S_8). Some studies have utilized microporous carbons with pore sizes ≤0.7 nm, which can accommodate only short-chain polysulfides (Li_2S_{2-4}) to resolve the challenge of polysulfide shuttling. However, the discharge products of long-chain polysulfides, Li_2S_8 and Li_2S_6 molecules with diameters of 0.84 nm and 0.76 nm, are not entirely confined in the micropores due to the poor affinity of the carbon host and polysulfides. In this study, we created microporous carbon (AC900) with a pore size of 1.2 nm that can accommodate both long and short-chain polysulfides and infiltrated it with sulfur (AC900S). To mitigate capacity fading, we further modified the carbon using urea (AC900NS) and nickel sulfate (AC900S-Ni) treatments. The latter did not result in detectable Ni incorporation but induced partial changes in carbon hybridization and surface structure. The synthesis-driven structural adjustment in AC900S-Ni influenced solid-state conversion and improved electrochemical stability compared to AC900S and AC900NS. The AC900S-Ni cathode demonstrated a capacity retention of 72% with a capacity of 773 mAh g_S^{-1} after 100 cycles and 1000 mAh g_S^{-1} in the first cycle at C/20, higher than those of AC900S and AC900NS. An improvement in capacity retention to 96% was noted at C/10, with a discharge capacity of 722 mAh g_S^{-1} after 100 cycles, compared to 805 mAh g_S^{-1} in the first cycle. The results identify the factor contributing to capacity fading in unmodified AC900S and demonstrate that chemical/structural modification of microporous carbon combined with a carbonate electrolyte provides a promising pathway for Li–S systems. This study offers a facile approach to tune carbon hosts and expand their applicability in Li–S batteries.

Received 5th February 2026,
Accepted 28th March 2026

DOI: 10.1039/d6ya00026f

rsc.li/energy-advances

1. Introduction

In recent decades, the development of green and sustainable energy sources has accelerated significantly. This progress has raised environmental concerns related to fossil fuels and the growing consumer demand for large commercial electric vehicles, as well as in aerospace and aviation.[1] Lithium–sulfur batteries (Li–S) have been considered a potential alternative to lithium-ion batteries (LIBs) in emerging high-power source devices due to their higher theoretical energy density (2600 Wh kg^{-1}) compared to their counterpart (300 Wh kg^{-1}) and the eco-friendly benefits of elemental sulfur.[2] However, the practical applications are limited by insufficient capacity retention during prolonged cycling, caused by instability at the lithium metal anode/electrolyte interface, structural instability of the sulfur cathode, and the diffusion of soluble polysulfides (Li_2S_n) from the cathode to the anode.[3–5]

Engineering microporous carbon with a pore size tailored to precisely accommodate sulfur molecules (C/S) is feasible, and an effective approach to confine the polysulfide intermediates within the carbon matrix to a certain degree.[6] This provides a rapid ion/electron transfer pathway, which improves sulfur utilization during the conversion reaction.[7] However, the challenge of achieving both high capacity and prolonged cycle life simultaneously remained largely unresolved.[8] Given the

[a] INM – Leibniz Institute for New Materials, Campus D2 2, 66123 Saarbrücken, Germany. E-mail: volker.presser@leibniz-inm.de
[b] National Institute of Chemistry, Hajdrihova 19, Ljubljana, Slovenia
[c] University of Salzburg, Department of Chemistry and Physics of Materials, Jakob-Haringer Straße 2a, 5020 Salzburg, Austria
[d] Department of Materials Science and Engineering, Saarland University, Campus D2 2, 66123 Saarbrücken, Germany
[e] saarene – Saarland Center for Energy Materials and Sustainability, Campus C4 2, 66123 Saarbrücken, Germany

non-polar nature of carbon and the corresponding weak interactions, polysulfides can still migrate out of the microporous carbons, leading to the loss of active material during charging/discharging over prolonged cycling.[9,10]

Metal-based compounds (transition metal oxides/hydroxides), which are characteristically polar materials like TiO_2,[11] Co_3O_4,[12] $Ni_3(NO_3)_2$,[13] and $Co(OH)_2$[14] are helpful as chemical trappers/blockers for polysulfides due to their strong surface polarity.[15,16] This enhances their interaction with polysulfides, maintaining Li–S cycling stability. However, the strong adsorption also results in the accumulation of inactive polysulfide species, which is fundamentally amplified by their low electrical conductivity.[17] This delays their ability to diffuse and transform polysulfides, leading to sluggish redox reactions.[18] Chemical modification of porous carbons using transition-metal-based catalysts, surface functionalization with nitrogen, and treatment with acid or alkaline solutions has proven promising.[19,20]

Catalysts enhance reaction kinetics through their strong chemisorption affinity for lithium polysulfide species, thereby maintaining structural stability and improving sulfur utilization.[21–23] However, the modification requires a robust design of the C/S composite, which is essential to guarantee performance and prevent the formation of undesirable side reactions that may result in dendrite formation and structural degradation. Furthermore, material production techniques and the compatibility of the C/S and chemical modifiers are essential in attaining precise control over the composite structure and properties.[23]

Additionally, state-of-the-art ether-based solvents exhibit higher solubility, supporting the decent reaction kinetics of intermediate polysulfide species.[24] However, the higher solubility also results in polysulfide diffusion from the cathode to the bulk electrolyte and anode, where they can react irreversibly. The increased polysulfide concentration increases the electrolyte viscosity, thereby reducing lithium mobility, resulting in rapid capacity fading or immediate cell death for lean electrolyte conditions (<3 μL mg_s^{-1}).[25] Using carbonate-based electrolytes in combination with microporous carbons could, in theory, circumvent these problems. These systems form a protective cathode electrolyte interphase (CEI) during the first discharge.[26] This prevents polysulfide dissolution and changes the conversion mechanism to a solid-state S/Li_2S conversion inside the micropore confinement. In a recent study, we hypothesized that poor charge-transfer kinetics during solid-state conversion are one of the significant capacity and rate-limiting factors.[27] Atomic-scale or nanoscale catalysts could, therefore, substantially improve performance, also during solid-state sulfur conversion in confinement.

In this study, we report a C/S composite electrode for Li–S batteries based on an optimized microporous carbon (AC900) engineered with a pore size of approximately 1.2 nm, capable of hosting both long- and short-chain polysulfides. Beyond structural optimization, we explored the effect of two chemical treatments, urea and nickel sulfate, on the electrochemical performance. We intended to deposit Ni on the carbon structure; however, the deposition was unsuccessful and unexpectedly altered the sp^2/sp^3 hybridization of the carbon, leading to significantly improved cycling stability. During synthesis, when nickel sulfate dissolves in water, it dissociates into hydrated nickel(II) ions and sulfate ions. Ammonia was used as a ligand to bind the nickel ion. Ammonia molecules replace the water molecules surrounding the nickel(II) ions to form nickel ammine complexes. Different characterization techniques did not detect Ni in our sample, suggesting that the complexes were removed during the washing process and that the Ni was separated from the solution. Yet, it still affected the sp^2/sp^3 ratio.

This work examines how these structural modifications affect sulfur confinement and electrochemical behavior in a carbonate-based electrolyte. Through structural characterization and electrochemical evaluation of AC900S, AC900NS, and AC900S-Ni, we identify how synthesis-induced changes to the carbon host can enhance long-term Li–S performance. The study provides new insight into microporous carbon design strategies and outlines a practical approach for improving polysulfide control in Li–S cathodes.

2. Experimental

2.1. Synthesis of materials and electrode preparation

The cathode material used for Li–S was produced through a heat treatment process followed by a simple chemical precipitation method. Firstly, YP50F (hereafter named AC0, from Kuraray Chemicals Co., Ltd) was activated at 900 °C for 1 h (heating rate of 5 °C min^{-1}) using a CO_2 flow of 100 mL min^{-1} in an aluminum-oxide tube furnace (Carbolite Gero). The tube was flushed with 100 mL min^{-1} of Ar during heating and cooling. The sample was abbreviated as AC900, and sulfur infiltration was performed as reported in our recent work.[28] The AC900 and sulfur (Sigma Aldrich) were mechanically mixed at a mass% ratio of 1 : 1 and ground in a ball mill using five balls (10 mm) at 300 rpm for 30 min. The mixture was then placed in a glass boat and heated under vacuum in a closed Büchi-Glass oven at 155 °C for 5 h; the sample was named AC900S.

Secondly, to mildly modify the surface hybridization or alter the sp^2/sp^3 ratio on the carbon surface of AC900S, nickel sulfate hexahydrate and an ammonia solution (a weak base) were used, following the method adjustment reported by Niu *et al.*[29] Here, 600 mg of AC900S and 95 mg of nickel sulfate hexahydrate were dispersed/dissolved in 90 mL of laboratory-grade water and stirred for 10 min. Ammonia solution (conc. 28%) was added, and the mixture was stirred for 1 h, followed by sonication for 30 min. After that, the sample was washed with deionized water (3 L) until the pH reached 7, then dried in an oven at 80 °C for 12 h. The final sample was called AC900S-Ni.

Third, AC900 was also functionalized with urea, which was used as a nitrogen source following an adjusted method reported by Schneidermann *et al.*[30] to compare the compatibility and performance of different modifications in the produced carbon. 1 g of AC900 and 5 g of urea were physically mixed and ball-milled at 300 rpm for 30 min. The sample was pyrolyzed in an Xerion furnace using a quartz glass tube at

850 °C for 1 h with a heating rate of 5 °C min^{-1} (Ar flow of 200 mL min^{-1}). The tube was flushed with 200 mL min^{-1} of Ar during heating and cooling. The sample was named AC900N. Sulfur infiltration was performed using the previously described method,[28] and the sample was designated as AC900NS. Sulfur infiltration was also performed in AC0 and used as a reference. The four samples, AC0S, AC900S, AC900NS, and AC900S-Ni, were used as cathode materials to study the influence of pore modification using CO_2 activation, surface functionalization, and structural modification on the prevention of polysulfide shuttling in lithium–sulfur batteries.

Electrodes were prepared by mixing the active material, conductive carbon C65 (Imerys), and polyvinylidene fluoride (PVDF, molecular mass approx. 534 000 g mol^{-1} from Sigma Aldrich) at a mass ratio of 8 : 1 : 1. *N*-Methyl-2-pyrrolidone (NMP, Sigma Aldrich) was added to prepare a slurry. The slurry was mixed with a ball mill at a speed of 300 rpm for 30 min and then doctor-bladed with an automatic coater (MTI Mini Cast Coater MSK-AFA-HC100) to spread the slurry on carbon-coated aluminum foil and dried in an oven at 80 °C for 12 h. The wet thickness was 200 μm, and the dried electrode attained a thickness of 80–90 μm with a mass loading of 3.0–3.4 mg cm^{-2} (normalized by 80% of the active material in a 10 mm in diameter circular disc punched with El-Cut), which corresponds to a sulfur loading of 1.6 ± 0.2 mg cm^{-2} and about 50 mass%.

2.2. Material characterization

The porous structure of the synthesized samples was determined using nitrogen gas sorption analysis (GSA) at −196 °C, performed using an Autosorb iQ system (Quantachrome; now Anton-Paar). Before analysis, the samples with an average mass of 0.03 g were degassed at 200 °C under vacuum for 12 h. The quenched solid density functional theory (QSDFT) was utilized to analyze the porosity, assuming a slit-shaped pore configuration. The average pore size was determined by the d_{50} value, which is the pore size equivalent to half of the pore volume.[31]

SAXS measurements of the bare AC900 microporous carbon, as well as the surface-modified and sulfur-infiltrated carbons (AC900N, AC900NS, and AC900S-Ni), were conducted on a Xeuss 3.0 laboratory SAXS system from Xenocs, equipped with Cu-Kα radiation (wavelength, λ = 0.154 nm), and the single photon counting detector Eiger 2R 1M from Dectris. The 2D SAXS intensities were azimuthally averaged and corrected for transmission, exposure time, and primary beam intensity.

We used a D8 discover diffractometer (Bruker AXS) equipped with a copper source (Cu Kα, 40 kV, 40 mA) for X-ray diffraction (XRD) analysis of the samples. The National Institute of Standards and Technology (NIST) 1976b corundum was used as a standard material to calibrate the X-ray beam before measurements. The measured signal was acquired using a 2D detector (VANTEC-500) and a Göbel mirror with a 1 mm point focus, in 0.02° 2θ steps, with 1 s per step. The powder was placed on an optical glass sample holder with a 0.5 mm deep notch for sample preparation.

A Renishaw inVia Raman microscope using an Nd-YAG laser with a 532 nm excitation wavelength and 0.5 mW power applied at the focal point of the sample using an objective lens with a numeric aperture of 0.75 was used to perform the Raman analysis. The 10 s exposure time was used to collect the spectra from 5 points per sample, which were accumulated 5 times. The spectra were treated with cosmic ray removal and normalized.

The surface micrographs were measured with a Zeiss Gemini 500 scanning electron microscope (SEM) at an acceleration voltage of 1 kV. An aluminum stub and copper tape were used as a substrate to attach the samples.

The carbon–sulfur samples were analyzed using XPS to investigate their surface properties. XPS analysis was conducted using a Versa probe 3 AD (Physical Electronics) with an Al-$K_{\alpha1}$ X-ray excitation source (1486.7 eV), operating monochromatically at 46.0 W. Measurements were performed at room temperature under high vacuum (10^{-7} Pa), and the spectra were acquired by scanning a 1 mm^2 area with a beam size of 200 μm. High-resolution spectra of carbon (C 1s) and sulfur (S 2p) were collected for detailed analysis. The pass energy and energy resolution were set to 27 eV and 0.05 eV for the core-level spectra. Voigt functions were used for spectral deconvolution, using Ulvac-PHI Multipak software, with Shirley background correction applied to all spectra. The binding energy scale was calibrated using Au $4f_{7/2}$ = 83.99 eV from pristine gold, which was sputtered for 7 min to remove possible impurities. Three regions were analyzed for each sample to ensure statistical accuracy and avoid potential single-point interpretations.

A bright-field scanning transmission electron microscope (BF-STEM) and a high-angle annular dark-field scanning transmission electron microscope (HAADF-STEM) from JEOL, Tokyo, Japan, were used to analyze the structure and composition of the carbon/sulfur samples. TEM samples were prepared by dispersing 0.1 mg of each powder in 4 mL of ethanol using an ultrasonic bath for 1 h, followed by the placement of 20 μL of the suspension on a copper TEM grid. The elemental mapping was performed by energy-dispersive X-ray spectroscopy in STEM mode (STEM-EDX). For these analyses, a probe aberration-corrected JEM-ARM200CF equipped with a JEOL Centurio 100 mm^2 EDXS detector and JEOL STEM detectors (JEOL, Tokyo, Japan) was employed.

Thermogravimetric analysis (TGA) was performed using a Netzsch TG-209-1 Libra system in the temperature range of 30–550 °C at a heating rate of 10 °C min^{-1}, with Ar gas used to analyze mass changes and measure sulfur loading. The ranges were selected as sulfur sublimates when heated to 450 °C at ambient pressure. The empty ceramic crucible container was weighed to determine its weight, which was then subtracted from the measurement to obtain the exact amount of the sample. After that, the powder was placed in the container for sample preparation and measurements.

The chemical composition of the samples was examined *via* CHNS-O analysis utilizing a Vario Micro Cube system (Elementar Analysenssteme). After combustion, the samples were measured in a combustion tube under an oxygen atmosphere at 1150 °C. Sulfanilic acid (C: 41.6 mass%, H: 4.1 mass%, N: 8.1 mass%,

and S: 18.5 mass%) was used to calibrate the CHNS-O analyzer measurements.

2.3. Electrochemical analysis

Li–S cells were fabricated using CR2032 coin cells (PI-KEM) to investigate the electrochemical performance of the as-synthesized cathode materials. Cells were assembled in an Ar-filled glove box (MBraun with O_2 and H_2O <0.1 ppm) using Li metal foil (MTI Corporation, 11 mm diameter, and 0.025 mm thickness) as the counter electrode and reference electrode with a Celgard 2320 separator (16 mm diameter). During cell assembly, 40 μL mg_S^{-1} of a carbonate-based electrolyte were used: 1 M $LiPF_6$ in fluoroethylene carbonate (FEC) and dimethyl carbonate (DMC) (in a 1 : 4 ratio by volume) ($LiPF_6$, FEC (99.99%) and DMC ($\geq$99%) were obtained from Sigma Aldrich). The galvanostatic charge/discharge experiments were performed to investigate the cycling stability in a Biologic VMP-300 potentiostat/galvanostat at C/20 in a voltage range of 0.5–3.0 V *vs.* Li/Li^+ for five formation cycles and then C/10 in a potential range of 1.0–3.0 V *vs.* Li/Li^+ in the subsequent cycles (1C = 1675 mAh g_S^{-1}). Further experiments were carried out at C/20 and C/10 (1C = 1675 mAh g_S^{-1}) independently in a voltage range of 1.0–3.0 V *vs.* Li/Li^+ for prolonged cycling to determine the effect of the C-rate on these cathodes. The galvanostatic intermittent titration technique (GITT) was performed with the following steps: a current (C/30) was applied for 15 min, followed by a relaxation time of 4 h. All electrochemical experiments were performed in a climate chamber held at 25 ± 1 °C. Unless specified otherwise, we calculated the capacity values based on the active material (sulfur). The Coulombic efficiency (CE) was calculated by dividing the discharge capacity by the previous charge capacity. Cyclic voltammetry was conducted within a potential range of 1.0–3.0 V *vs.* Li/Li^+ at a scan rate of 0.1 mV s^{-1}. In contrast, electrochemical impedance spectroscopy (EIS) was carried out at open-circuit voltage (OCV) over a frequency range from 10 kHz to 10 mHz. The cells were allowed to rest for 2 h prior to the EIS measurements.

3. Results and discussion

3.1. Textural/structural properties

Nitrogen gas sorption analysis (GSA) was performed at −196 °C on AC900, AC900N, AC900S, AC900NS, and AC900S-Ni samples and the results are shown in the SI, Fig. S1A and Fig. 1A. All samples confirmed micropore dominance, with AC900 exhibiting a larger pore volume than AC0 (SI, Fig. S1B and C). Fig. 1A presents the pore size distributions calculated using the QSDFT model assuming slit pores at equilibrium (Table 1). The DFT-specific surface

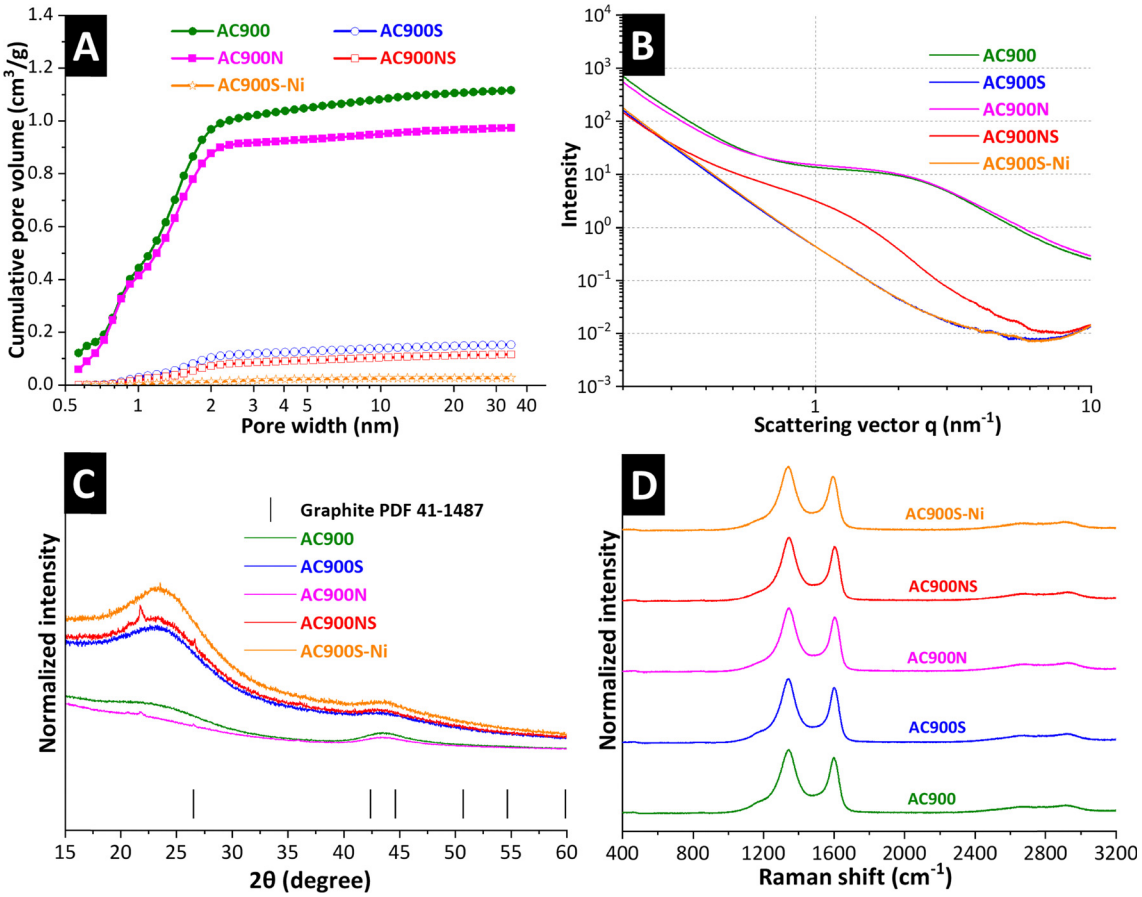

Fig. 1 Calculated pore size distributions derived from nitrogen gas sorption (A), small-angle X-ray scattering intensity *versus* scattering vector length *q* (B), X-ray diffraction pattern (C), and (D) Raman analysis of AC900, AC900S, AC900N, AC900NS, and AC900S-Ni, respectively.

Table 1 Surface and pore structure analysis of the AC0, AC900, AC900S, AC900N, AC900NS, and AC900S-Ni samples

Sample name	DFT SSA ($m^2\ g^{-1}$)	Average pore size d_{50} (nm)	Micropore volume ($cm^3\ g^{-1}$)	Mesopore volume ($cm^3\ g^{-1}$)	Total pore volume ($cm^3\ g^{-1}$)
AC0	1610	0.8	0.67	0.07	0.74
AC900	2057	1.2	0.97	0.15	1.12
AC900S	186	1.5	0.10	0.05	0.15
AC900N	1799	1.1	0.88	0.10	0.98
AC900NS	132	1.7	0.07	0.04	0.12
AC900S-Ni	31	2.0	0.01	0.01	0.03

areas (SSA) measured for AC0 and AC900 were 1610 $m^2\ g^{-1}$ and 2057 $m^2\ g^{-1}$. AC0 has an average pore size of 0.8 nm (total pore volume 0.74 $cm^3\ g^{-1}$), which increased to 1.2 nm (total pore volume 1.12 $cm^3\ g^{-1}$) after CO_2 activation (AC900). The CO_2 activation was intended to produce a microporous carbon with a pore size that can accommodate both long-chain polysulfides (Li_2S_8-0.84 nm and Li_2S_6-0.76 nm) and short-chain polysulfides (Li_2S_{2-4}-$<$0.5 nm). The DFT SSA and pore volume of AC900 decreased to 186 $m^2\ g^{-1}$ and 0.15 $cm^3\ g^{-1}$ after sulfur infiltration, indicating that sulfur occupied all the pores. This decrease demonstrates the adsorption and retention of elemental sulfur in the micropores of AC900S.[32]

Despite the ability of micropores in combination with carbonate-based electrolytes to confine polysulfides, with extended cycling polysulfide species can still migrate out of the pores and cause capacity fading due to poor charge transfer kinetics during solid-state conversion.[27,33] To avoid this, we attempted to modify the surface of our micropore carbon (AC900) using two different chemical processes: urea, used as a nitrogen source (AC900NS), and nickel sulfate (AC900S-Ni). The purpose was to understand the performance behavior of polysulfide suppression in prolonged cycling for this carbon and its compatibility with different chemical or surface structural modifications. The nitrogen was introduced into the surface of the micropores to increase the adsorption of polysulfides, boost electrical conductivity,[34] and potentially transfer charge across the carbon/active material interface. Due to its chemical adsorption properties, nickel sulfate was used as a catalyst to modify the micropore surface, facilitating electrochemical reactions.[35] The DFT SSA of the nitrogen-modified sample (AC900N) was 1799 $m^2\ g^{-1}$ (total pore volume 0.98 $cm^3\ g^{-1}$), which is less than that of AC900 (2057 $m^2\ g^{-1}$ *vs.* 1.12 $cm^3\ g^{-1}$). The pore volume was reduced after sulfur infiltration to 0.12 $cm^3\ g^{-1}$ (AC900NS). The sample, which we attempted to modify with nickel sulfate (AC900S-Ni), presented a DFT SSA and pore volume of 31 $m^2\ g^{-1}$ and 0.03 $cm^3\ g^{-1}$ (less than those of AC900S with 186 $m^2\ g^{-1}$ *vs.* 0.15 $cm^3\ g^{-1}$; Table 1).

SAXS analysis was carried out to verify changes in the nanopore structure upon surface modifications and sulfur infiltration. Fig. 1B displays the SAXS intensity as a function of the scattering vector length q of AC900, AC900S, AC900N, AC900NS, and AC900S-Ni samples. The pronounced hump in the SAXS intensity of the empty activated carbon is characteristic of its nanopore structure.[36] The AC900 and AC900N samples show identical SAXS intensities with a pronounced shoulder around 2 nm^{-1}–3 nm^{-1}, indicative of the mean pore size around $\pi/q \approx 1.2\ nm^{-1}$. The decreasing SAXS intensity of the sulfur-infiltrated samples (AC900S, AC900NS, and AC900S-Ni) provides evidence that the sulfur effectively blocks the carbon nanopores.[37] Upon sulfur infiltration, the scattering-length-density contrast between the pore and the carbon matrix decreases, leading to the disappearance of the nanopore shoulder. Interestingly, the AC900N (nitrogen-modified sample) shows no statistically significant effect on the nanopore structure, whereas the sample attempted to be modified with nickel sulfate (AC900S-Ni) exhibits a visible shoulder around 1 nm^{-1}, indicative of the structural change within the pores.[27]

Fig. 1C presents the X-ray diffractograms of AC900, AC900S, AC900N, AC900NS, and AC900S-Ni. All samples exhibited two disordered carbon peaks at 24° and 43° 2θ, corresponding to the diffraction at the (002) and (100) planes, respectively (PDF number 41-1487).[38] The incorporation of nitrogen in the AC900 carbon leads to a slight decrease in the peak intensity of the 24° 2θ value of the AC900N (Fig. 1C). Sulfur infiltration increases the intensity around 24° 2θ due to the superposition of the carbon at the (002) planes and an amorphous sulfur peak. AC900S-Ni exhibits a slightly more pronounced peak around 24° 2θ. The absence of sharp crystalline sulfur peaks indicates that amorphous sulfur is confined in the micropores.[39]

The samples were further analyzed by Raman spectroscopy, as presented in Fig. 1D. The Raman analysis for AC900, AC900S, AC900N, AC900NS, and AC900S-Ni revealed the D band, indicating a disordered aromatic structure of sp^3-bonded carbon, and the G band related to the sp^2 stretching bond of graphite (SI, Table S1).[40] The D- and G-band, together with their full width at half maximum (FWHM), were obtained by fitting the spectra using Voigt peak profile analysis. The AC900 presented a D band at 1344 cm^{-1} with a FWHM of 126 cm^{-1} and a G band at 1596 cm^{-1} with a FWHM of 74 cm^{-1}. The defect created by sulfur infiltration into AC900 was revealed by the decreased intensity of the D band for AC900S at 1340 cm^{-1} and FWHM of 115 cm^{-1} (G band: 1599 cm^{-1}; FWHM: 68 cm^{-1}), indicating sulfur was infiltrated into the micropore carbon. The AC900N displayed a D band at 1345 cm^{-1} with a FWHM of 116 cm^{-1} and a G band at 1601 cm^{-1} with a FWHM of 69 cm^{-1}. There is no significant change after sulfur infiltration, as the AC900NS recorded almost similar values (D band: 1344 cm^{-1}; FWHM: 116 cm^{-1}; G band: 1601 cm^{-1}; FWHM: 69 cm^{-1}). However, the introduction of nitrogen into the micropores of AC900 results in small structural distortion,[41] as confirmed by the decrease in FWHM (SI, Table S1, AC900: 126 cm^{-1} *vs.* AC900N: 116 cm^{-1}). In addition, the AC900S-Ni recorded a D band at 1339 cm^{-1} with a FWHM of 120 cm^{-1} and a G band at 1591 cm^{-1} with a FWHM of 75 cm^{-1}. The defects created by nickel sulfate modification were indicated by a slight increase in the FWHM of AC900S-Ni, at 120 cm^{-1} compared to AC900S at 115 cm^{-1} (SI, Table S1).[42]

The same characteristics and behavior of the absence of sulfur in the XRD analysis in Fig. 1C were also confirmed in the Raman analysis in Fig. 1D. Further confirmation was observed

in the scanning electron micrographs in the SI, Fig. S2A–E. The images show comparable morphologies, with the same shape and size for AC900, AC900S, AC900N, AC900NS, and AC900S-Ni, despite chemical modification and sulfur infiltration. This also confirms that sulfur was integrated into the micropores.

Both XRD and Raman demonstrate that no new peak associated with nickel was formed for the AC900S-Ni; however, structural changes in the carbon framework, indicative of modified sp^2 (graphitic) ordering, were observed due to the wet-chemical nickel sulfate treatment on the AC900-S. This was confirmed by XPS analysis of AC900-S, AC900NS, and AC900S-Ni. High-resolution C 1s spectra for the AC900S, AC900NS and AC900S-Ni samples are presented in the SI, Fig. S3A, C, and in E. Seven distinct peaks can be identified,[43] with the peak at 284.7 eV corresponding to sp^2 hybridized graphitic carbon, while the peak at 285.0 eV is attributed to sp^3 hybridized carbon or C–H bonds. Four additional peaks are associated with various oxygen-containing functional groups, and a final peak at 292.2 eV corresponds to the π–π^* transition.[44] The relative contributions of each species are summarized in Table 2. The most notable difference between the two samples lies in the sp^2/sp^3 carbon ratios. The AC900S-Ni sample exhibits 73 atom% sp^2 carbon, representing a 16 atom% increase compared to the AC900S sample. This enhancement is primarily due to a corresponding 16 atom% reduction in sp^3 content, indicating a significant degree of graphitization induced by the nickel sulfate washing procedure. In contrast, the relative abundance of oxygenated species remains nearly unchanged between the two materials. The interpretation of the AC900NS is not straightforward due to the overlap with nitrogen-containing species. Specifically, contributions from C–H and C–N (pyridinic N), C–O and C═N (pyrrolic N), and C═O with N–CO (graphitic N) can complicate peak assignment. To resolve this, high-resolution N 1s spectra were also acquired (SI, Fig. S4). Three main peaks are observed: one at 398.5 eV corresponding to pyridinic N, another at 400.2 eV assigned to pyrrolic N, and a third at 401.9 eV attributed to graphitic nitrogen species.[45,46] However, the latter could also be associated with oxidized N, given the uncertainty caused by the signal-to-noise ratio in the spectrum. In addition, the high-resolution S 2p spectra for the AC900S, AC900NS and AC900S-Ni samples are shown in the SI, Fig. S2B, D and F, indicating the presence of C–S (~163–164 eV), S–O species (166–169 eV), and elemental sulfur (~164 eV).[33,47]

Table 2 Binding atom% content of different C-species in AC900S, AC900NS, and AC900S-Ni, as shown in the SI, Fig. S3A, C and E

	Content of C species (atom%)		
Species	AC900S	AC900NS	AC900S-Ni
C sp^2	57	63	73
C sp^3/C–N	25	14	9
C–O/C═N	6	5	4
C–O–C	6	7	6
O–C–O/C═O/N–C═O	3	6	4
O–C═O	3	4	4

The absence of nickel and structural modification caused by the nickel sulfate washing process was further confirmed by the BF-STEM and HAADF-STEM analyses performed on the AC900S and AC900S-Ni samples. BF-STEM was used to provide information about the morphology, porosity, crystal structure, and the arrangement of carbon and sulfur in the samples.[48] At the same time, HAADF-STEM was employed to identify the elemental composition and distribution within the sample, as well as its morphology.[49] Fig. 2A, B and D, E display the BF-STEM images at low and high magnification of AC900S and AC900S-Ni, respectively. The morphology consisted of disordered graphitic layers, characterized by closely packed, frizzy carbon layers that enclosed coordinated pores. The dark area (carbon) and bright area (sulfur) of the HAADF-STEM image on AC900S (Fig. 2C) and AC900S-Ni (Fig. 2F) confirm the sulfur distribution and dispersion within the carbon matrix. The AC900S-Ni shows a more uniform sulfur distribution when compared to AC900S, as heavier elements in the sample appear brighter than lighter ones based on Rutherford scattering, which intensifies with an increase in atomic number (Z).[50] The TEM-EDS elemental mapping (SI, Fig. S5A and E) shows the presence of carbon, oxygen, and sulfur in AC900S (SI, Fig. S5B–D) and AC900S-Ni (SI, Fig. S5F–H). The TEM-EDS spectra for AC900S and AC900S-Ni (SI Fig. S5I) show similar elemental compositions with no presence of nickel in AC900S-Ni. The most distinctive feature between the two samples is that sulfur is more evenly distributed in AC900S-Ni (SI, Fig. S5H) compared to AC900S (SI Fig. S5D). This also agrees with the HAADF-STEM image of AC900S-Ni (Fig. 2F).

In general, to elucidate the structural changes caused by the nickel sulfate treatment, we observe that transient exposure to Ni^{2+} ions can enhance graphitic ordering, even when no residual Ni is found in the final material. *In situ* investigations have revealed that Ni promotes the transformation of amorphous carbon into a domain rich in sp^2 bonding *via* dissolution–precipitation and carbide-mediated mechanisms.[51] This process involves the formation and subsequent breakdown of transient Ni_3C upon heating, thereby promoting the development of graphitic layers at comparatively low temperatures and leaving no residual nickel in the final material.[51] Transition-metal ions, including Ni^{2+}, are known to temporarily bind to oxygen- and sulfur-containing surface groups, thereby reducing the activation barriers for local carbon rearrangement and favoring short-range ordering toward sp^2-rich domains during subsequent drying or mild heating.[52] Furthermore, Ni^{2+} can interact with defect sites and regions rich in heteroatoms, thereby enabling partial defect repair and restoring conjugated carbon networks, thereby increasing the sp^2/sp^3 ratio. The transient formation of Ni–S or Ni–O coordination complexes may further modify the carbon–sulfur interface; their removal during washing results in a more ordered carbon structure.[52] These catalytic activities and defect-reconstruction pathways are consistent with the broader observation that Ni layers or Ni-containing intermediates accelerate graphitization by enhancing carbon mobility and enabling the reorganization of disordered carbon networks into more ordered graphitic structures.[53] These

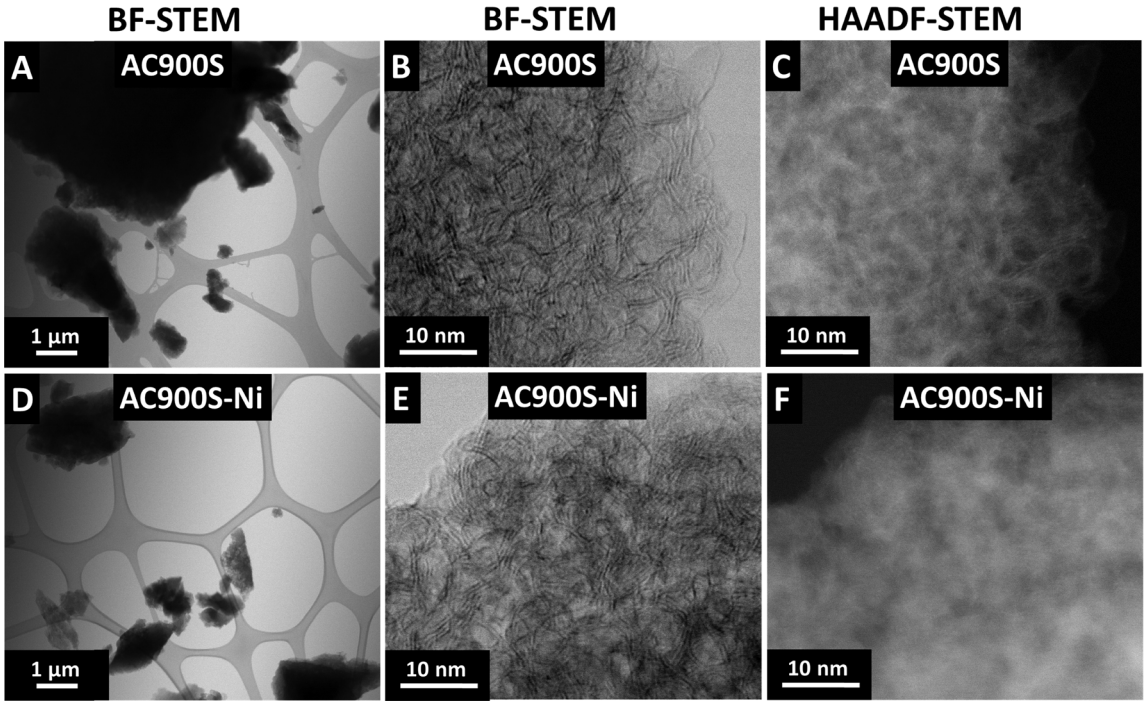

Fig. 2 Low and high-resolution BF-STEM analysis of AC900S (A) and (B) and AC900S-Ni (D) and (E), respectively. High-resolution HAADF-STEM analysis of AC900S (C) and AC900S-Ni (F).

provide a mechanistic explanation for the observed enhancement in sp^2 characteristic, despite the absence of detectable Ni in the final composite.

The sulfur content infiltrated in the micropores was determined by TGA measurements performed in the 30–550 °C range using argon gas (SI, Fig. S6). At and beyond 450 °C, the sulfur was expected to be fully vaporized. Still, it did not appear that way, as it was trapped in the microporous carbon and required more energy for assembly and evaporation. The defect created on the surface of the micropores by nickel sulfate modification (AC900S-Ni) was also observed in the TGA analysis, where the complete evaporation begins at 500 °C, compared to 470 °C for AC900S and AC900NS. The C/S ratio was 1 : 1 and the sulfur content recorded was 47 mass%, 48 mass%, and 47 mass% for AC900S, AC900NS and AC900S-Ni, respectively. This amount was also confirmed by CHNS-O analysis (Table 3) to be around 50 mass% for all samples. AC900S, AC900NS, and AC900S-Ni showed a mass-loading for sulfur with 51 mass%, 49 mass%, and 48 mass%, respectively. The oxygen content was below 3 mass% for AC900N, AC900NS, and AC900S-Ni. The nitrogen content measured in the samples was approximately 2 mass% for AC900N and AC900NS.

3.2. Electrochemical analysis of lithium–sulfur batteries

3.2.1. Influence of CO_2 activation on the pore structure for small and large-chain polysulfide confinement. Fig. 3A–D presents the electrochemical measurements of AC0S and AC900S performed using 1 M $LiPF_6$ in FEC/DMC (1 : 4 by volume) carbonate-based electrolyte. The AC0S and AC900S were cycled using C/20 (1C = 1675 mAh g_S^{-1}) in a potential range of 0.5–3.0 V *vs.* Li/Li^+ for 5 formation cycles to attain equilibrium after the CEI formation, followed by C/10 in a potential range of 1.0–3.0 V *vs.* Li/Li^+ for the proceeding cycles. The absence of two distinct voltage plateaus and the general shape of the charge/discharge profile clearly speak for solid-state S/Li_2S conversion.[27] The AC0S recorded a discharge capacity of 1018 mAh g_S^{-1}, 909 mAh g_S^{-1}, 841 mAh g_S^{-1}, and 788 mAh g_S^{-1} for cycles one to four at C/20 (Fig. 3A). The discharge capacity decreased to

Table 3 Chemical composition of the non-infiltrated carbons and sulfur-infiltrated carbons. The value of *S* mass loss from the TGA is calculated from the difference between the mass remaining and the original (100%)

	CHNS-O analysis (mass%)					TGA (mass%)
Sample name	C	N	H	O	S	*S*
AC900	94.58 ± 1.91	—	0.34 ± 0.08	—	—	—
AC900N	83.64 ± 1.17	1.94 ± 0.03	0.25 ± 0.07	3.22 ± 0.62	—	—
AC900S	47.57 ± 0.62	—	≤0.2	—	51.02 ± 1.24	47
AC900NS	43.72 ± 0.53	1.15 ± 0.02	0.21 ± 0.06	1.88 ± 0.01	49.36 ± 0.43	48
AC900S-Ni	48.43 ± 0.53	0.49 ± 0.04	—	2.42 ± 0.20	48.04 ± 0.34	47

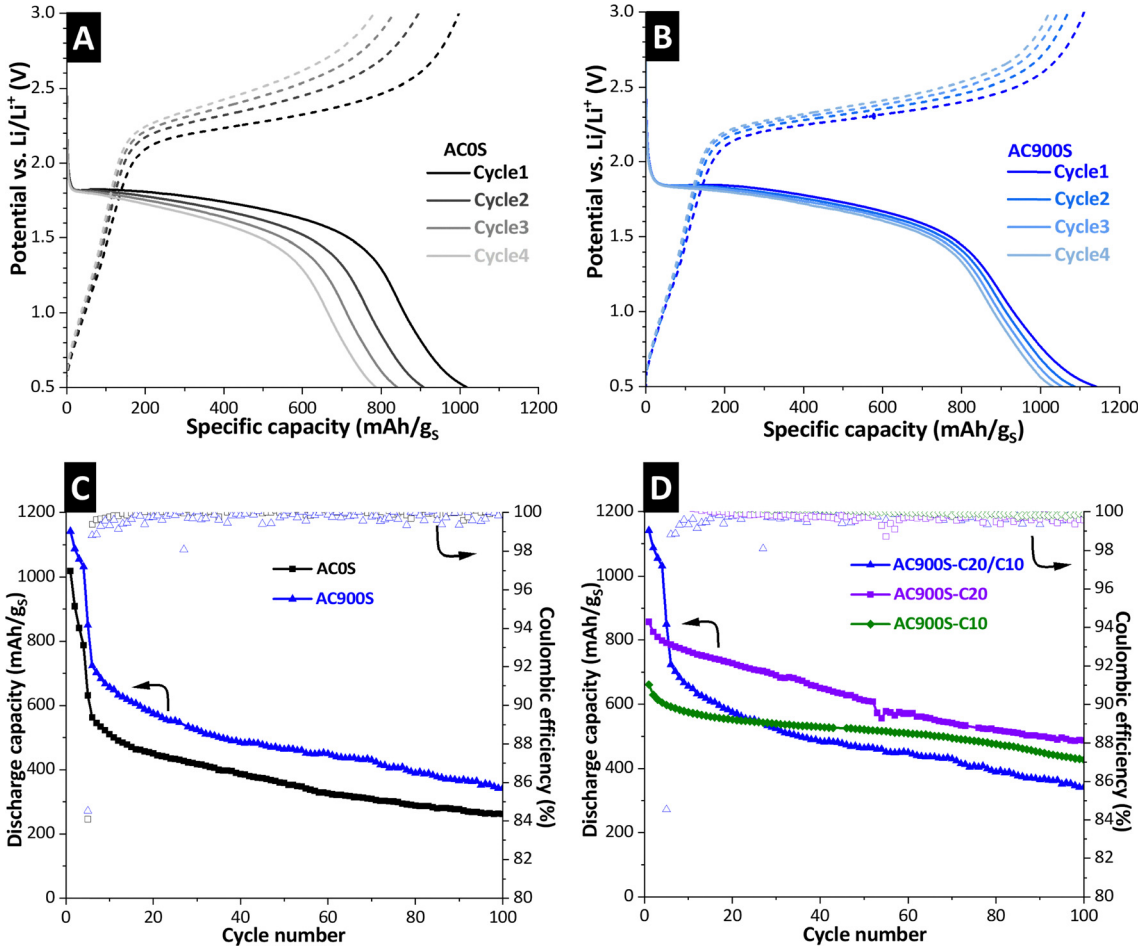

Fig. 3 The charging and discharging of cycles one to four for the CO_2-activated carbon AC900S and AC0S without activation measured at 0.5–3.0 V *vs.* Li/Li^+ (A) and (B). The cycling stability and Coulombic efficiency of AC900S and AC0S measured at 0.5–3.0 V *vs.* Li/Li^+ with C/20 for five formation cycles, followed by 1.0–3.0 V *vs.* Li/Li^+ with C/10 for up to 100 cycles (C). The cycling stability and Coulombic efficiency of AC900S measured at 1.0–3.0 V *vs.* Li/Li^+ with C/20 and C/10 (the AC900S-C20/C10 represents AC900S and 1C = 1675 mAh g_S^{-1}) (D).

631 mAh g_S^{-1} once switched to a higher cycling current (C/10), and a discharge capacity of 261 mAh g_S^{-1} remained after 100 cycles (Fig. 3C). The AC900S, on the other hand, displayed a discharge capacity of 1142 mAh g_S^{-1}, 1088 mAh g_S^{-1}, 1056 mAh g_S^{-1}, and 1032 mAh g_S^{-1} for cycles one to four at C/20 (Fig. 3B). The discharge capacity decreased to 850 mAh g_S^{-1} when switched to a higher current (C/10), and a discharge capacity of 342 mAh g_S^{-1} remained after 100 cycles (Fig. 3C). These values are shown in the SI, Table S2. The AC900S sample exhibited a higher initial discharge capacity (1142 mAh g_S^{-1}-C/20 *vs.* 850 mAh g_S^{-1}-C/10) compared to the AC0S sample (1018 mAh g_S^{-1}-C/20 *vs.* 631 mAh g_S^{-1}-C/10). The higher performance of AC900S is also reflected in its volumetric capacity, as shown in the SI, Fig. S7B. It also attained better cycling stability than its counterpart (Fig. 3C). Our data indicate that the additional activation step on AC0 enhances the AC900 properties for efficient sulfur conversion. This could be due to the polarity, surface functional groups, and hydrophobicity.[54] The additional pore space from CO_2 activation likely improves the transport of solvated electrolyte and lithium ions, which is crucial for sustaining the high reversible capacity of the sulfur cathode.[55]

Although the microporous nature resulted in reduced side reactions[56] and confined reactions between polysulfide species and carbonates, continuous capacity fading was observed during the extended cycling of AC900S. This suggests that AC900S has a weak chemical affinity with polysulfides, and therefore, it cannot entirely trap them and prevent capacity fading.[33] Since AC900S exhibits micropores that can accommodate both long- and short-chain polysulfides, it still experiences capacity fading. We first investigate the effect of cycling conditions on the capacity fading. This was analyzed in the next section.

3.2.2. Effect of cycling conditions on the polysulfide shuttle suppression. As AC900S displayed an initial discharge of 850 mAh g_S^{-1} once switched to a higher cycling current of C/10 (1.0–3.0 V *vs.* Li/Li^+), it was expected to cycle around 800 mAh g_S^{-1} for the subsequent cycles; however, it experienced continued capacity fading in the following cycles. To understand this phenomenon in our cathode (AC900S), we performed two independent measurements at C/20 and C/10 (1C = 1675 mAh g_S^{-1}) in a potential range of 1.0–3.0 V *vs.* Li/Li^+. The purpose was to determine if switching to a higher current

and potential simultaneously, once the CEI has formed and the cathode has stabilized, contributes to continuous capacity fading.

Fig. 3D shows the cycling stability of AC900S performed at C/20 and C/10 without switching the currents and potential. The effect of the cycling condition is observed between the cathode (AC900S-C20/C10) measured by switching the current and potential (C/20 with 0.5–3.0 V *vs.* Li/Li^+ for 5 formation cycles, followed by C/10 with 1.0–3.0 V *vs.* Li/Li^+ for the proceeding cycles), and without switching the currents/potential (AC900S-C/20 and AC900S-C/10 with 1.0–3.0 V *vs.* Li/Li^+). The AC900S-C/20 recorded an initial discharge capacity of 857 mAh g_S^{-1}, 612 mAh g_S^{-1} after 50 cycles, with 488 mAh g_S^{-1} remaining after 100 cycles. The AC900S-C/10 presented an initial discharge capacity of 661 mAh g_S^{-1}, 521 mAh g_S^{-1} after 50 cycles, with 428 mAh g_S^{-1} remaining after 100 cycles. AC900S cycled at C/20 and C/10 showed improved discharge capacity and better cycling stability than the AC900S cycled by simultaneously switching the current/potential C20/C10 (Fig. 3D). These results indicate that, in the micropore, the highly dispersed short-chain configurations of low-molecular-weight elemental sulfur are unstable due to the low potential difference *versus* metallic lithium compared to the larger molecules of elemental sulfur with crown ring structures.[57,58] Additionally, electrode degradation and electrolyte decomposition occur in the less stable electrochemical reaction zone, which is also influenced by the battery's charge/discharge potential.[59] Thus, the simultaneous change of current and potential might have influenced the observed performance in the AC900S cathode cycled at C20/C10.

Based on these results (Fig. 3D), we were able to reduce the capacity fading; however, our cathode (AC900S) still exhibits slow capacity fading in subsequent cycles, indicating that the reactions between polysulfides and carbonates are not entirely confined to the micropores. To further understand the behavior of polysulfides in our micropore, the following section details the mechanism of polysulfide suppression using a carbonate electrolyte, aided by surface/structural modifications on the microporous carbon. We created chemical affinity in our microporous carbon (AC900) and investigated the influence of surface modification and the structural compatibility of this carbon with various chemical modifications. Additionally, in Fig. 3D, we observe the effects of simultaneously switching the C-rate and potential in our cathode. Consequently, the remaining measurements in this study were performed at C/20 and C/10 (1.0–3.0 V *vs.* Li/Li^+) independently, without simultaneously switching the current and potential.

3.2.3. Impact of structural compatibility between the produced carbon and surface modifier. This section describes the electrochemical performance of Li–S using an AC900 carbon modified by two different chemical modifications. The modification was made to create a strong affinity for polysulfide, thereby improving capacity fading in extended cycling.

Fig. 4A shows the initial discharge profiles of AC900S, AC900NS, and AC900S-Ni performed at C/20 in a potential range of 1.0–3.0 V *vs.* Li/Li^+ in 1 M $LiPF_6$ in FEC/DMC (1 : 4 by volume) carbonate-based electrolyte. All cathodes presented the formation of two potential plateaus with different characteristics. The first plateau appears at 2.4 V *vs.* Li/Li^+ for AC900S and AC900NS, and at 2.2 V *vs.* Li/Li^+ for AC900S-Ni. The plateau is associated with the reduction of sulfur to high-order polysulfide (Li_2S_n, $4 < n < 8$) and the reaction between carbonate solvent molecules and the carbon host.[7,60] The second plateau appears at 1.69 V *vs.* Li/Li^+ for AC900S, and at 1.7 V *vs.* Li/Li^+ for the AC900NS and AC900S-Ni, respectively. The second plateau is linked with the formation of lower-order polysulfides (Li_2S_2 and Li_2S).[61] The behavior of these plateaus is consistent with the discharge potential of sulfur confined in microporous carbon using a carbonate-based electrolyte, confirming a solid–solid conversion process.[62] The AC900S-Ni presented a distinctive feature in the length of the second plateau, as it was terminated at 1.03 V *vs.* Li/Li^+ with a slightly higher cut-off potential of 0.03 V *vs.* Li/Li^+, compared to the set potential of 1.0 V *vs.* Li/Li^+.

The characteristics of the initial discharge profiles for AC900S, AC900NS, and AC900S-Ni were also analyzed at a higher C-rate of C/10 using a potential range of 1.0–3.0 V *vs.* Li/Li^+ as exhibited in Fig. 4B. The cathodes displayed the formation of two plateaus with characteristics similar to those observed at a lower C-rate of C/20 (Fig. 4A). The first plateau was observed at 2.3 V *vs.* Li/Li^+ for AC900NS and AC900S-Ni and at 2.2 V *vs.* Li/Li^+ for AC900S. The second plateau for AC900NS is at 1.66 V *vs.* Li/Li^+, and for AC900S and AC900S-Ni is at 1.63 V *vs.* Li/Li^+. Similar characteristics of the second plateau termination at a higher cut-off potential of 1.01 V *vs.* Li/Li^+ *versus* the set potential of 1.0 V *vs.* Li/Li^+ were observed for the AC900S-Ni (Fig. 4B). The cyclic voltammograms of AC900S, AC900NS, and AC900S-Ni show redox peaks (SI, Fig. S8A), signifying a solid–solid conversion route from S to Li_2S and further confirming the behavior of the plateaus, as shown in Fig. 4A and B.

Fig. 4C and D display the subsequent charge/discharge profiles of AC900S, AC900NS, and AC900S-Ni in a potential range of 1.0–3.0 V *vs.* Li/Li^+ with C/20 and C/10, respectively. Fig. 4C shows an improvement in the discharge capacity for the chemical-modified cathodes (AC900NS and AC900S-Ni) measured with C/20 (1C = 1675 mAh g_S^{-1}). The discharge capacities in the first cycle were 857 mAh g_S^{-1}, 946 mAh g_S^{-1}, and 1000 mAh g_S^{-1} for AC900S, AC900NS, and AC900S-Ni, respectively. Similar performance improvement was recorded when the cathodes were cycled at a higher current of C/10 with a potential range of 1.0–3.0 V *vs.* Li/Li^+ (Fig. 4D). The discharge capacities in the first cycle were 661 mAh g_S^{-1}, 770 mAh g_S^{-1}, and 805 mAh g_S^{-1} for AC900S, AC900NS, and AC900S-Ni, respectively.

Fig. 4E and F display the cycling stability of AC900S, AC900NS, and AC900S-Ni in a potential range of 1.0–3.0 V *vs.* Li/Li^+ with C/20 and C/10, respectively. The sample modified with nitrogen (AC900NS) exhibited improved performance compared to AC900S, displaying a higher discharge capacity of up to 65 cycles at C/20 (Fig. 4E) and 200 cycles at C/10 (Fig. 4F). Introducing nitrogen as a polar functional group with higher electronegativity was intended to effectively enhance the interfacial interaction between polysulfides and the surface of

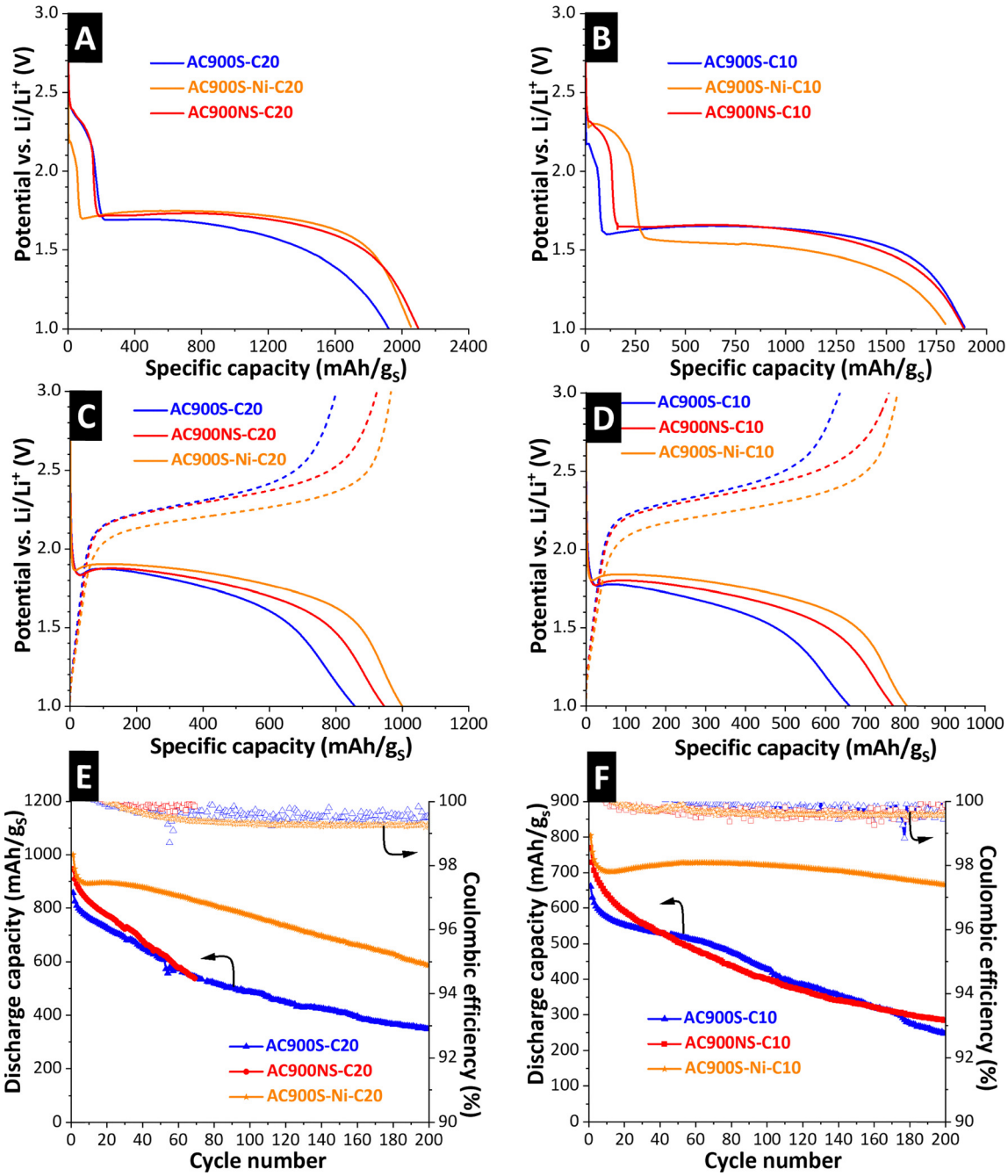

Fig. 4 The initial discharge of AC900S, AC900NS, and AC900S-Ni measured at 1.0–3.0 V *vs.* Li/Li^+ with C/20 (A) and C/10 (B). The first charge/discharge of AC900S, AC900NS, and AC900S-Ni measured at 1.0–3.0 V *vs.* Li/Li^+ with C/20 (C) and C/10 (D). The cycling stability and Coulombic efficiency of AC900S, AC900NS, and AC900S-Ni performed at 1.0–3.0 V *vs.* Li/Li^+ with C/20 (C) and C/10 (D).

the micropore carbon (AC900).[63] Theoretically, the nitrogen atom exhibits an extra pair of electrons and is recognized as an electron-rich donor (pyridinic/pyrrolic N),[64] as confirmed with our XPS analysis of the N 1s spectra (SI, Fig. S4). These serve as Lewis-base sites, interacting with the strong Lewis acidity of the terminal lithium atoms in lithium polysulfides through dipole–dipole electrostatic interactions.[8] Meanwhile, graphitic N acts as an electron donor, donating additional electrons to adjacent delocalized π-systems. This leads to a stronger affinity for polysulfides compared to the graphene plane.[65] The initial enhancement in our AC900NS aligns with the secondary effects typically associated with low levels of pyridinic and pyrrolic nitrogen functionalities, which can slightly increase surface polarity and provide limited additional anchoring interactions for polysulfides. However, the extent of these improvements remains small, and the long-term cycling performance does not significantly differ from that of the unmodified sample (AC900S). These results support the idea

that nitrogen plays only a minor supportive role in the overall electrochemical response, as a continuous decrease in the discharge capacity was noted in the subsequent cycles of AC900NS (Fig. 4E and F). Previous research shows that increased nitrogen content or specific nitrogen functionalities can enhance the adsorption and confinement of polysulfides by improving surface polarity and strengthening chemical interactions. For example, a study on urea-doped activated carbon indicates that higher nitrogen levels, achieved by increasing the urea ratio, significantly enhance polysulfide adsorption capacity. The sample with higher nitrogen doping showed the highest polysulfide uptake, due to the combined effects of high porosity and pronounced nitrogen functionalization.[66] Furthermore, the active pyridinic and pyrrolic sites in nitrogen-doped functionalized hollow carbon nanocages were shown to promote stronger sulfur immobilization and polysulfide trapping, confirming that specific N functionalities, like pyridinic and pyrrolic structures, enhance chemical interactions with lithium polysulfide species.[67]

AC900S-Ni cycled at C/20 showed better cycling stability, with the cathode retaining a discharge capacity of 773 mAh g_S^{-1} after 100 cycles, 587 mAh g_S^{-1} after 200 cycles (Fig. 4E), and 455 mAh g_S^{-1} after 270 cycles (SI, Fig. S7C) compared to 1000 mAh g_S^{-1} in the first cycle. A similar improvement was observed on the AC900S-Ni cycled at C/10, which retained discharge capacities of 722 mAh g_S^{-1} after 100 cycles, 665 mAh g_S^{-1} after 200 cycles (Fig. 4F), and 354 mAh g_S^{-1} after 500 cycles (SI, Fig. S7D) compared to 805 mAh g_S^{-1} in the first cycle. The improvement was also noted in the Coulombic efficiency performance, whereby AC900S-Ni cathodes exhibited a stable Coulombic efficiency at both cycling currents, in contrast to the unstable Coulombic efficiency of AC900S and AC900NS (Fig. 4E and F). The Nyquist plots (SI, Fig. S8B) indicate a significant difference in charge-transfer resistance (R_{ct}) across AC900S, AC900NS, and AC900S-Ni. AC900S shows a smaller semicircle, aligning with more favorable charge transfer during the solid-state conversion. AC900NS exhibits the largest semicircle, indicating the highest R_{ct} and suggesting that nitrogen doping in this configuration slightly hinders electronic transport and interfacial kinetics,[68] consistent with the long-term cycling performance shown in Fig. 4E and F. AC900S-Ni exhibits the smallest semicircle, indicating that the nickel sulfate post-treatment, despite leaving no residual nickel, effectively reduces R_{ct} by enhancing the sp^2-bonded carbon and improving electronic pathways.[69] The steeper low-frequency tail of AC900S-Ni further supports easier Li^+ transport and a more reversible solid-state conversion under carbonate–electrolyte conditions.

GITT was performed to further elucidate the performance enhancement of AC900S-Ni. The total polarization as a function of state-of-discharge (SoD) and state-of-charge (SoC) is presented in the SI, Fig. S9A and B, and the GITT pulse is presented in the SI, Fig. S9C. Decoupling the individual contributions to polarization (ohmic, charge transfer, and mass transport) remains challenging because both charge transfer and mass transport exhibit prolonged relaxation times in sulfur confined within microporous carbon cathodes. Nevertheless, AC900S-Ni demonstrates reduced polarization during both discharge and charge processes, with a notable decrease of approximately 0.05 V in total polarization. This improvement is most likely attributable to enhanced charge transfer kinetics, corroborated by the significant increase in sp^2-hybridized graphitic carbon content observed *via* XPS analysis (SI, Fig. S3E, Table 2). The higher graphitic carbon content facilitates electron transfer and accelerates the solid-state conversion reactions of polysulfide species. Furthermore, Fig. S9B in the SI reveals critical insights into the delithiation process, which appears to be the primary performance-limiting factor for this battery system. Beyond 60% SoC during charging, the polarization exceeds 0.5 V, whereas during discharge (lithiation), the polarization remains relatively constant at approximately 0.25 V. This disparity suggests that delithiation kinetics impose a significant constraint on the overall electrochemical performance.

In general, the nitrogen-doping process appears to alter the pore-formation pathway, leading to a slight reduction in accessible porosity and a shift in pore distribution (Fig. 1A and Table 1). This phenomenon aligns with findings that indicate nitrogen inclusion can affect the activation chemistry and modify pore development in nitrogen-doped porous carbon.[70] At the same time, the electronic properties of the carbon matrix are notably affected by the specific nitrogen configurations present. Research comparing organic-N and inorganic-N doping shows that pyridinic and pyrrolic nitrogen improve conductivity, whereas inorganic nitrogen species may reduce it, thereby decreasing charge-transfer efficiency.[68] These combined reductions in pore accessibility and electronic conductivity provide a coherent explanation for the decreased sulfur utilization and less effective long-term cycling of AC900NS, which dominate the slight early-cycle benefits associated with low levels of nitrogen functionalities. Meanwhile, the enhanced electrochemical performance of the AC900S-Ni sample can be attributed mainly to its higher sp^2/sp^3 carbon ratio, as observed in the SI, Fig. S3E, and Table 2. The increase in sp^2-hybridized carbon, along with a significant reduction in sp^3 and C–H bonds, contributes to reduced polarization and improved charge-transfer kinetics, as confirmed by the GITT analysis.[44] In contrast, sp^3-hybridized carbon and C–H groups not only lower electronic conductivity but also introduce non-polar, hydrophobic regions.[71,72] These hydrophobic surfaces can hinder electrolyte wetting and penetration, potentially blocking pore entrances or reducing the effective pore volume, which ultimately limits sulfur utilization, as observed in the AC900S sample. Moreover, sp^3-rich domains impair the redox kinetics of polysulfide conversion by reducing electrical conductivity, which slows down Li_2S formation.[73] Additionally, studies indicate that graphitic sp^2 carbon offers more robust adsorption sites for polysulfide intermediates, while sp^3-rich carbon shows weaker interactions.[74,75] This diminished affinity may indirectly promote the dissolution and loss of polysulfides, further hindering overall conversion efficiency for the AC900S sample.

Compared to the state-of-the-art ether-based electrolyte utilizing $LiNO_3$ to improve Coulombic efficiency in microporous carbon, the battery typically operates in a potential range of

1.7–2.8 V *vs.* Li/Li^+ (1.1 V *vs.* Li/Li^+).[76] Our battery exhibited improved performance at a higher operating potential of 1.0–3.0 V *vs.* Li/Li^+ (2.0 V *vs.* Li/Li^+) utilizing a surface-modified microporous carbon (AC900S-Ni cathode) in a carbonate-based electrolyte. This electrolyte has been less used for Li–S systems due to the side reactions that occur between carbonates and polysulfides. Additionally, carbonate-based electrolytes are more mature and stable *vs.* Li metal as they are already used in Li-ion batteries and also offer a lower cost compared to ether-based electrolytes.

4. Conclusions

We have investigated and successfully reduced the continued slow capacity fading during extended cycling in microporous carbon using a carbonate-based electrolyte, which is less commonly used in Li–S systems. Some studies have used microporous/ultra-microporous carbon with pore sizes of ≤ 0.7 nm, which can accommodate only the short-chain polysulfides LiS_{2-4}.[6,77] The discharge products of long-chain polysulfides, LiS_8 and Li_2S_6 molecules with pore sizes of 0.84 nm and 0.76 nm, are limited in the microporous carbon. The pore size of the micropore carbon used in this study (1.2 nm) was optimized to a range that can accommodate both long-chain and short-chain polysulfides. Furthermore, the carbon was modified to potentially create an improved chemical affinity for polysulfides and improved charge transfer kinetics, resulting in reduced capacity fading. The modification was performed using urea as a nitrogen source (AC900NS) and nickel sulfate as a nickel source (AC900S-Ni). Different characterization techniques did not detect Ni in our sample, suggesting that it was removed during the washing process; however, this still alters the sp^2/sp^3 ratio, which in turn affects the electronic properties of this sample. Using a carbonate electrolyte, the AC900S-Ni achieved better cycling stability in subsequent cycles compared to AC900S. Overall, our results demonstrate that chemical/structural modification of the internal carbon surface can reduce capacity fading during solid-state S/Li_2S conversion in confinement using microporous carbons and a carbonate electrolyte.

Author contributions

DJT: conceptualization, methodology, investigation, data curation, validation, visualization, writing – original draft, review and editing. FJGS: conceptualization, investigation, data curation, validation, review and editing. AV: conceptualization, investigation, data curation, validation, funding acquisition, review and editing. CP: investigation, data curation, validation, review and editing. ET: investigation, data curation, validation, review and editing. VP: conceptualization, validation, data curation, funding acquisition, review and editing.

Conflicts of interest

The authors have no conflicts of interest.

Data availability

Supplementary information (SI) is available (gas sorption data, scanning electron micrographs, X-ray photoelectron spectra, elemental mapping/transmission electron microscopy, thermogravimetric analysis, electrochemical data, Raman spectroscopy data, electrochemical performance data). See DOI: https://doi.org/10.1039/d6ya00026f.

All data can be accessed *via* https://doi.org/10.5281/zenodo.19048044.

Acknowledgements

The INM authors acknowledge the German Federal Ministry for Research and Education (BMBF) and Slovenia Research Foundations (MIZS) for funding the joint M-ERA.NET ALISA project (PR-457221). Andrea Jung (INM) is acknowledged for performing the CHNS-O analysis. DJT acknowledges funding from the Alexander von Humboldt Foundation. Additionally, A. V. and E. T. acknowledge the financial support from the Slovenian Research and Innovation Agency (ARIS) under the research core program P2-0423 and project GC-0004.

References

1 S. Arnold, J. G. Ruthes, C. Kim and V. Presser, *EcoMat*, 2024, e12494.
2 M. Fichtner, K. Edström, E. Ayerbe, M. Berecibar, A. Bhowmik, I. E. Castelli, S. Clark, R. Dominko, M. Erakca, A. A. Franco, A. Grimaud, B. Horstmann, A. Latz, H. Lorrmann, M. Meeus, R. Narayan, F. Pammer, J. Ruhland, H. Stein, T. Vegge and M. Weil, *Adv. Energy Mater.*, 2022, **12**, 2102904.
3 P. G. Bruce, S. A. Freunberger, L. J. Hardwick and J.-M. Tarascon, *Nat. Mater.*, 2012, **11**, 19–29.
4 J.-G. Wang, K. Xie and B. Wei, *Nano Energy*, 2015, **15**, 413–444.
5 C. X. Bi, N. Yao, X. Y. Li, Q. K. Zhang, X. Chen, X. Q. Zhang, B. Q. Li and J. Q. Huang, *Adv. Mater.*, 2024, **36**, 2411197.
6 L. Hu, Y. Lu, X. Li, J. Liang, T. Huang, Y. Zhu and Y. Qian, *Small*, 2017, **13**, 1603533.
7 Z. Li, L. Yuan, Z. Yi, Y. Sun, Y. Liu, Y. Jiang, Y. Shen, Y. Xin, Z. Zhang and Y. Huang, *Adv. Energy Mater.*, 2014, **4**, 1301473.
8 T. Z. Hou, X. Chen, H. J. Peng, J. Q. Huang, B. Q. Li, Q. Zhang and B. Li, *Small*, 2016, **12**, 3283–3291.
9 X. Ji, S. Evers, R. Black and L. F. Nazar, *Nat. Commun.*, 2011, **2**, 325.
10 M. Agostini and A. Matic, *Small*, 2020, **16**, 1905585.
11 Z. W. Seh, W. Li, J. J. Cha, G. Zheng, Y. Yang, M. T. McDowell, P.-C. Hsu and Y. Cui, *Nat. Commun.*, 2013, **4**, 1331.
12 X. Liang, C. Y. Kwok, F. Lodi-Marzano, Q. Pang, M. Cuisinier, H. Huang, C. J. Hart, D. Houtarde, K. Kaup, H. Sommer, T. Brezesinski, J. Janek and L. F. Nazar, *Adv. Energy Mater.*, 2016, **6**, 1501636.

13 J. Jiang, J. Zhu, W. Ai, X. Wang, Y. Wang, C. Zou, W. Huang and T. Yu, *Nat. Commun.*, 2015, **6**, 8622.
14 X.-q Niu, X.-l Wang, D.-h Wang, Y. Li, Y.-j Zhang, Y.-d Zhang, T. Yang, T. Yu and J.-p Tu, *J. Mater. Chem. A*, 2015, **3**, 17106–17112.
15 D. J. Tarimo, K. O. Oyedotun, A. A. Mirghni, N. F. Sylla and N. Manyala, *Electrochim. Acta*, 2020, **353**, 136498.
16 X. Liu, J. Q. Huang, Q. Zhang and L. Mai, *Adv. Mater.*, 2017, **29**, 1601759.
17 J. Balach, J. Linnemann, T. Jaumann and L. Giebeler, *J. Mater. Chem. A*, 2018, **6**, 23127–23168.
18 S. Liu, J. Li, X. Yan, Q. Su, Y. Lu, J. Qiu, Z. Wang, X. Lin, J. Huang, R. Liu, B. Zheng, L. Chen, R. Fu and D. Wu, *Adv. Mater.*, 2018, **30**, 1706895.
19 T. Tang and Y. Hou, *Small Methods*, 2020, **4**, 1900001.
20 E. Cha, M. Patel, S. Bhoyate, V. Prasad and W. Choi, *Nanoscale Horiz.*, 2020, **5**, 808–831.
21 G. Zhou, S. Zhao, T. Wang, S.-Z. Yang, B. Johannessen, H. Chen, C. Liu, Y. Ye, Y. Wu, Y. Peng, C. Liu, S. P. Jiang, Q. Zhang and Y. Cui, *Nano Lett.*, 2019, **20**, 1252–1261.
22 C.-X. Bi, L.-P. Hou, Z. Li, M. Zhao, X.-Q. Zhang, B.-Q. Li, Q. Zhang and J.-Q. Huang, *Energy Mater. Adv.*, 2023, **4**, 0010.
23 S. F. Ng, M. Y. L. Lau and W. J. Ong, *Adv. Mater.*, 2021, **33**, 2008654.
24 L. Suo, Y.-S. Hu, H. Li, M. Armand and L. Chen, *Nat. Commun.*, 2013, **4**, 1481.
25 A. Varzi, K. Thanner, R. Scipioni, D. Di Lecce, J. Hassoun, S. Dörfler, H. Altheus, S. Kaskel, C. Prehal and S. A. Freunberger, *J. Power Sources*, 2020, **480**, 228803.
26 R. Dominko, A. Vizintin, G. Aquilanti, L. Stievano, M. J. Helen, A. R. Munnangi, M. Fichtner and I. Arcon, *J. Electrochem. Soc.*, 2017, **165**, A5014.
27 A. Senol Gungor, J.-M. von Mentlen, J. G. A. Ruthes, F. J. García-Soriano, S. Drvarič Talian, V. Presser, L. Porcar, A. Vizintin, V. Wood and C. Prehal, *ACS Appl. Mater. Interfaces*, 2024, **16**, 67651–67661.
28 D. J. Tarimo, F. J. García-Soriano, A. Vizintin, C. Prehal and V. Presser, *ACS Appl. Energy Mater.*, 2025, **8**, 12139–12156.
29 X.-Q. Niu, X.-L. Wang, D. Xie, D.-H. Wang, Y.-D. Zhang, Y. Li, T. Yu and J.-P. Tu, *ACS Appl. Mater. Interfaces*, 2015, **7**, 16715–16722.
30 C. Schneidermann, C. Kensy, P. Otto, S. Oswald, L. Giebeler, D. Leistenschneider, S. Grätz, S. Dörfler, S. Kaskel and L. Borchardt, *ChemSusChem*, 2019, **12**, 310–319.
31 G. Y. Gor, M. Thommes, K. A. Cychosz and A. V. Neimark, *Carbon*, 2012, **50**, 1583–1590.
32 W. Feng, S. Kwon, E. Borguet and R. Vidic, *Environ. Sci. Technol.*, 2005, **39**, 9744–9749.
33 Y. Xu, Y. Wen, Y. Zhu, K. Gaskell, K. A. Cychosz, B. Eichhorn, K. Xu and C. Wang, *Adv. Funct. Mater.*, 2015, **25**, 4312–4320.
34 K. Xiang, S. Cai, X. Wang, M. Chen and S. Jiang, *J. Alloys Compd.*, 2018, **740**, 687–694.
35 H. Wu, Y. Li, J. Ren, D. Rao, Q. Zheng, L. Zhou and D. Lin, *Nano Energy*, 2019, **55**, 82–92.
36 C. Prehal, S. Grätz, B. Krüner, M. Thommes, L. Borchardt, V. Presser and O. Paris, *Carbon*, 2019, **152**, 416–423.
37 F. J. Garcia-Soriano, J. Jerovsek, S. A. Maldonado-Ochoa, F. Vaca Chavez, D. J. Tarimo, V. Presser, B. Genorio, M. Florent, T. J. Bandosz, R. Dominko, C. Prehal and A. Vizintin, *ACS Appl. Energy Mater.*, 2025, **9**, 211–221.
38 J. Y. Howe, C. J. Rawn, L. E. Jones and H. Ow, *Powder Diffr.*, 2003, **18**, 150–154.
39 V. V. Shinkarev, V. B. Fenelonov and G. G. Kuvshinov, *Carbon*, 2003, **41**, 295–302.
40 A. Sadezky, H. Muckenhuber, H. Grothe, R. Niessner and U. Pöschl, *Carbon*, 2005, **43**, 1731–1742.
41 H. Chen, F. Sun, J. Wang, W. Li, W. Qiao, L. Ling and D. Long, *J. Phys. Chem. C*, 2013, **117**, 8318–8328.
42 P. Xia, W. Lei, X. Wang, Z. Luo, Y. Pan and Z. Ma, *J. Alloys Compd.*, 2020, **832**, 153692.
43 R. Blume, D. Rosenthal, J. P. Tessonnier, H. Li, A. Knop-Gericke and R. Schlögl, *ChemCatChem*, 2015, **7**, 2871–2881.
44 F. J. García-Soriano, F. Cometto, S. Raviolo, T. Slosar, E. Tchernychova, B. Genorio, R. Dominko, M. V. Bracamonte and A. Vizintin, *Commun. Mater.*, 2025, **6**, 122.
45 Y. Chen, C. Zhang, C. Li, T. Gao, Y. Li, Y. Jiang, J. Niu, M. Zhang and S. Yao, *Carbon*, 2026, 121354.
46 Y. Wang, E. Indubala, C. Ma, C. Zhang, L. Xiao, B. Lv and S. Yao, *J. Energy Storage*, 2025, **121**, 116575.
47 D. Zalka, A. Vizintin, A. Maximenko, Z. Pászti, Z. Dankházi, K. Hegedüs, L. S. Shankar, R. Kun, K. Saksl, A. S. Fedorková and P. Jóvári, *Commun. Mater.*, 2025, **6**, 17.
48 M. J. Zachman, Z. Yang, Y. Du and M. Chi, *ACS Nano*, 2022, **16**, 1358–1367.
49 K. Sohlberg, T. J. Pennycook, W. Zhou and S. J. Pennycook, *Phys. Chem. Chem. Phys.*, 2015, **17**, 3982–4006.
50 Y. Kotaka, T. Yamazaki, M. Ohtsuka and K. Watanabe, *Ultramicroscopy*, 2014, **136**, 119–126.
51 J. Kim, S. Son, M. Choe and Z. Lee, *Mater. Today Adv.*, 2024, **22**, 100494.
52 H. Rastegar and E. Mansorizadeh, *Carbon Lett.*, 2022, **32**, 835–848.
53 G. B. Choi, J.-R. Ahn, J. Kim, T. H. Seo and S. W. Lee, *ACS Omega*, 2024, **9**, 6741–6748.
54 N. S. Devi, M. Hariram and S. Vivekanandhan, *J. Energy Storage*, 2021, **33**, 101870.
55 J. Chmiola, G. Yushin, Y. Gogotsi, C. Portet, P. Simon and P.-L. Taberna, *Science*, 2006, **313**, 1760–1763.
56 J. Gao, M. A. Lowe, Y. Kiya and H. D. Abruna, *J. Phys. Chem. C*, 2011, **115**, 25132–25137.
57 N. Xu, T. Qian, X. Liu, J. Liu, Y. Chen and C. Yan, *Nano Lett.*, 2017, **17**, 538–543.
58 G. Li, S. Wang, Y. Zhang, M. Li, Z. Chen and J. Lu, *Adv. Mater.*, 2018, **30**, 1705590.
59 M. L. Para, C. A. Calderón, S. Drvarič Talian, F. Fischer, G. L. Luque, D. E. Barraco, E. P. M. Leiva and R. Dominko, *Batteries Supercaps*, 2022, **5**, e202100374.
60 Z. Li, Y. Jiang, L. Yuan, Z. Yi, C. Wu, Y. Liu, P. Strasser and Y. Huang, *ACS Nano*, 2014, **8**, 9295–9303.

61 Q. Zhu, Q. Zhao, Y. An, B. Anasori, H. Wang and B. Xu, *Nano Energy*, 2017, **33**, 402–409.
62 B. Zhang, X. Qin, G. R. Li and X. P. Gao, *Energy Environ. Sci.*, 2010, **3**, 1531–1537.
63 W. He, X. He, M. Du, S. Bie, J. Liu, Y. Wang, M. Liu, Z. Zou, W. Yan and H. Zhao, *J. Phys. Chem. C*, 2019, **123**, 15924–15934.
64 H. J. Peng, T. Z. Hou, Q. Zhang, J. Q. Huang, X. B. Cheng, M. Q. Guo, Z. Yuan, L. Y. He and F. Wei, *Adv. Mater. Interfaces*, 2014, **1**, 1400227.
65 Y. Xia, R. Fang, Z. Xiao, H. Huang, Y. Gan, R. Yan, X. Lu, C. Liang, J. Zhang, X. Tao and W. Zhang, *ACS Appl. Mater. Interfaces*, 2017, **9**, 23782–23791.
66 M. S. Md Zaini, S. A. M. Al-Junid and S. S. A. Syed-Hassan, *J. Porous Mater.*, 2024, **31**, 831–842.
67 C. Ma, Z. Zheng, X. Jia, X. Liu, J. Wang, W. Qiao and L. Ling, *J. Power Sources*, 2021, **486**, 229358.
68 Q. Fan, Z. Li, Y. Sun, C. Song and P. Fu, *J. Mater. Sci.*, 2024, **59**, 13043–13054.
69 C.-S. Cheng and S.-H. Chung, *Chem. Eng. J.*, 2022, **429**, 132257.
70 B. Pérez-Román, J. López-Sánchez, M. A. Mazo and F. Rubio-Marcos, *Coord. Chem. Rev.*, 2026, **551**, 217330.
71 L. Ostrovskaya, V. Perevertailo, V. Ralchenko, A. Dementjev and O. Loginova, *Diamond Relat. Mater.*, 2002, **11**, 845–850.
72 K. Meng, Z. Zhang, X. Tan and Q. Yu, *Diamond Relat. Mater.*, 2021, **120**, 108609.
73 C. Prehal, J.-M. von Mentlen, S. Drvarič-Talian, A. Vizintin, R. Dominko, H. Amenitsch, L. Porcar, S. A. Freunberger and V. Wood, *Nat. Commun.*, 2022, **13**, 6326.
74 J. Guo, Y. Xu and C. Wang, *Nano Lett.*, 2011, **11**, 4288–4294.
75 X. Liang, C. Hart, Q. Pang, A. Garsuch, T. Weiss and L. F. Nazar, *Nat. Commun.*, 2015, **6**, 5682.
76 S. S. Zhang, *J. Power Sources*, 2013, **231**, 153–162.
77 H. M. Joseph, T. Diemant, S. Schindler, J. R. Behm, M. Danzer, U. Kaiser, M. Fichtner and M. A. Reddy, *ACS Omega*, 2018, **3**, 11290–11299.